machines

MDPI

Article

PFC-Based Control of Friction-Induced Instabilities in Drive Systems

Ievgen Golovin [1,*] and Stefan Palis [1,2]

[1] Institute for Automation Engineering, Otto von Guericke University Magdeburg, 39106 Magdeburg, Germany; stefan.palis@ovgu.de
[2] Department of Electric Power Systems, National Research University "Moscow Power Engineering Institute", 111250 Moscow, Russia
* Correspondence: ievgen.golovin@ovgu.de; Tel.: +49-391-67-51506

Abstract: This paper is concerned with control-based damping of friction-induced self-excited oscillations that appear in electromechanical systems with an elastic shaft. This approach does not demand additional oscillations measurements or an observer design. The control system provides the angular velocity and damping control via the combination of a parallel feed-forward compensator (PFC) and adaptive λ-tracking feedback control. The PFC is designed to stabilize the zero dynamics of an augmented system and renders it almost strict positive real (ASPR). The proposed control approach is tested in simulations.

Keywords: parallel feed-forward compensator; λ-tracking control; friction-induced oscillations; velocity control

check for updates

Citation: Golovin, I.; Palis, S. PFC-Based Control of Friction-Induced Instabilities in Drive Systems. *Machines* **2021**, *9*, 134. https://doi.org/10.3390/machines9070134

Academic Editors: Khoa D Hoang, Nigel Schofield and Essam Hussain

Received: 22 June 2021
Accepted: 13 July 2021
Published: 16 July 2021

Publisher's Note: MDPI stays neutral with regard to jurisdictional claims in published maps and institutional affiliations.

Copyright: © 2021 by the authors. Licensee MDPI, Basel, Switzerland. This article is an open access article distributed under the terms and conditions of the Creative Commons Attribution (CC BY) license (https://creativecommons.org/licenses/by/4.0/).

1. Introduction

A number of friction effects appear in different machines and mechanisms driven by automated electric drive systems. It is well known that friction may deteriorate performance of feedback control loops. This may also result in oscillatory dynamics and large steady-state errors during closed-loop operation and typically leads to increased mechanical wear [1–4]. Friction characteristics with dropping regions are particularly negative, i.e., negative slope regions of friction torque-velocity characteristics. Here, by operation in these regions, friction-induced stick-slip or self-excited oscillations may appear. This problem is common for various areas: cranes, rolling mills, industrial robots, railways, vehicles, aircraft engines, rolling element bearings, drilling systems, etc. [5–12]. To solve the problem of these nonlinear oscillations, a number of control-based approaches have been presented in the literature, e.g., PD control [13,14], linear robust control [15], indirect adaptive control [16], feedback linearization [17], sliding-mode control [18], and backstepping control [19]. In the majority of the works, it is considered that oscillations in a working element of the mechanism or machine can be measured or estimated.

In this paper, a new approach for damping the friction-induced self-excited oscillations is proposed. This approach does not require an additional measurement system on the working element side and can be easily integrated in classical motion control systems without their full redesign. This makes this method valuable from a practical point of view. The proposed control system is based on a combination of a parallel feed-forward compensator (PFC) and λ-tracking controller. Its effectiveness is verified using the simulation model. The problem of friction-induced self-excited vibrations is studied on the example of a two-mass electromechanical system with an elastic shaft. The system is considered to be driven by an electric drive. It will be shown that, during operation in the negative slope region, not only the system dynamics becomes unstable, but its zero dynamics becomes unstable too, i.e., the nonminimum phase. From a theoretical point of view, application of feedback control to this class of systems is a challenging task, as they are known to

be unstable under high controller gains. In order to provide stability of the closed-loop system, at first, parallel feed-forward interconnection of a plant and compensator [20–24] is applied, which results in an augmented system with a redefined output and stable zero dynamics. After this, the augmented system dynamics is stabilized applying adaptive λ-tracking control [25]. It should be mentioned that the proposed PFC design also renders the augmented plant almost strict positive real (ASPR) [23,24], hence the basis for other control approaches as well.

Section 2 presents the distributed parameter mathematical model of the two-mass electromechanical system with an elastic shaft and its discretization. In Section 3, the problem of occurrence of friction-induced self-excited vibrations is shown. Section 4 introduces the design of a PFC and control law. In Section 5, the proposed control system is evaluated in a simulation study. Section 6 summarizes the results presented in this paper and gives an outlook for future work.

2. Modeling

2.1. Mathematical Model

In this contribution, a prototypic rotatory two-mass electromechanical system with an elastic shaft, as illustrated in Figure 1, is considered [12,26]. Here, the drive torque $\tau_m(t)$ actuates the first mass and the load friction torque τ_{fr} is subjected to the second mass. The electromechanical system can be described by the following hyperbolic partial differential equation (PDE)

$$\ddot{\varphi}(z,t) = \frac{G}{\rho}\,\varphi''(z,t) - \frac{\gamma}{\rho I}\,\dot{\varphi}(z,t) \tag{1}$$

with two boundary conditions

$$GI\,\varphi'(0,t) = J_1\,\ddot{\varphi}(0,t) + \beta\,\dot{\varphi}(0,t) - \tau_m(t), \tag{2}$$

$$GI\,\varphi'(L,t) = -J_2\,\ddot{\varphi}(L,t) - \tau_{fr}\big(\dot{\varphi}(L,t)\big). \tag{3}$$

Here, $\varphi(z,t)$ is the rotational angle of the shaft, which depends on the spatial coordinate $z \in (0, L)$ and time t, $\varphi(0,t) = \varphi_0$ is the rotational angle of the first mass, i.e., the motor, $\varphi(L,t) = \varphi_L$ is the rotational angle of the second mass, J_1 and J_2 are the first and second masses' moments of inertia, β is the coefficient of viscous friction subjected to the first mass, G and I are the shear modulus and the moment of inertia of the shaft, and ρ and γ are the density and structural damping of the shaft. The prime $'$ and dot $\dot{}$ symbols denote the spatial and time derivatives, respectively.

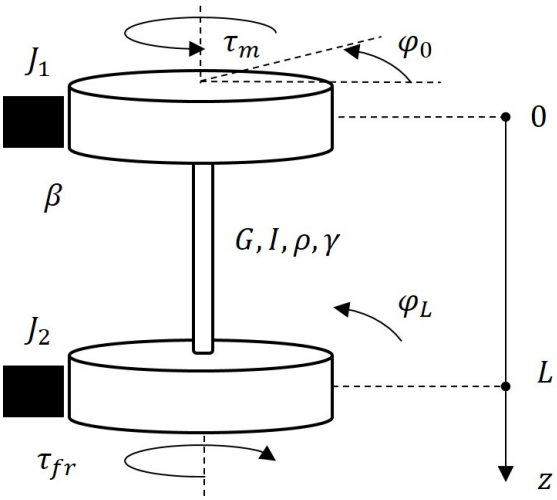


Figure 1. Electromechanical system.

In this contribution, friction load curves possessing a negative slope region are of particular interest as they may cause instability and the occurrence of limit cycles. Therefore, the following friction model is utilized [1]

$$\tau_{fr} = \tau_{co}\tanh(k_{fr}\,\dot{\varphi}_L) + \tau_{vi}\,\dot{\varphi}_L + (\tau_{st} - \tau_{co})\,e^{-|\dot{\varphi}_L/b_{sb}|}\tanh(k_{fr}\,\dot{\varphi}_L), \tag{4}$$

where τ_{co} is the Coulomb friction torque, τ_{vi} is the viscous dissipation torque, τ_{st} is the static friction torque, b_{sb} is the empirical parameter characterizing the Stribeck effect, k_{fr} is the adjustable parameter of the slope in the region of zero velocity.

It is assumed that the electric drive operates in the current (torque) control mode. Its fast closed-loop dynamics can be typically neglected, and, thus, the motor torque can be considered as a control input $u(t) = \tau_m(t)$.

2.2. Model Discretization

For simulation and control design, the presented infinite-dimensional electromechanical model is discretized. Here, the method of lines has been applied [27]. Therefore, the spatial coordinate of the PDE (1) is discretized by applying a finite difference approximation with $n = 100$ grid points

$$\varphi'(z,t)\Big|_{z=z_i} \approx \frac{-\varphi_{i-1} + \varphi_{i+1}}{2h}, \tag{5}$$

$$\varphi''(z,t)\Big|_{z=z_i} \approx \frac{\varphi_{i-1} - 2\varphi_i + \varphi_{i+1}}{h^2}, \tag{6}$$

where $h = z_{i+1} - z_i$ is the distance between two grid points and φ_i is the value of φ at grid node i.

Substituting the approximations (5) and (6) into (1)–(3) and solving the equations with respect to their highest time derivatives, the following matrix equation results

$$\ddot{\varphi} = S\varphi + R\dot{\varphi} + B_u u + B_{fr}\tau_{fr}\left(\dot{\varphi}_L\right). \tag{7}$$

Here, the stiffness $S \in \mathbb{R}^{(n+1)\times(n+1)}$, damping $R \in \mathbb{R}^{(n+1)\times(n+1)}$, control input $B_u \in \mathbb{R}^{(n+1)\times 1}$, and friction torque $B_{fr} \in \mathbb{R}^{(n+1)\times 1}$ matrices are calculated as follows:

$$S = \frac{G}{\rho h^2}\begin{bmatrix} -2b_1 & 2b_1 & 0 & \cdots & 0 & 0 & 0 \\ 1 & -2 & 1 & \cdots & 0 & 0 & 0 \\ 0 & 1 & -2 & \cdots & 0 & 0 & 0 \\ \vdots & \vdots & \vdots & \ddots & \vdots & \vdots & \vdots \\ 0 & 0 & 0 & \cdots & -2 & 1 & 0 \\ 0 & 0 & 0 & \cdots & 1 & -2 & 1 \\ 0 & 0 & 0 & \cdots & 0 & 2b_2 & -2b_2 \end{bmatrix},\; B_u = \frac{2}{\rho h I}\begin{bmatrix} b_1 \\ 0 \\ 0 \\ \vdots \\ 0 \\ 0 \\ 0 \end{bmatrix},$$

$$R = -\frac{\gamma}{\rho I}\begin{bmatrix} d_1 & 0 & \cdots & 0 & 0 \\ 0 & 1 & \cdots & 0 & 0 \\ 0 & 0 & \cdots & 0 & 0 \\ \vdots & \vdots & \ddots & \vdots & \vdots \\ 0 & 0 & \cdots & 1 & 0 \\ 0 & 0 & \cdots & 0 & d_2 \end{bmatrix},\; B_{fr} = -\frac{2}{\rho h I}\begin{bmatrix} 0 \\ 0 \\ \vdots \\ 0 \\ 0 \\ b_2 \end{bmatrix},$$

where

$$b_1 = \frac{\rho h I}{\rho h I + 2J_1},\; b_2 = \frac{\rho h I}{\rho h I + 2J_2},\; d_1 = b_1\left[\frac{2\rho\beta h}{\gamma G} + 1\right],\; d_2 = b_2\,.$$

By defining the additional angular velocity vector $\omega = \dot{\varphi} = [\omega_0, \ldots, \omega_L]^T \in \mathbb{R}^{(n+1)}$ and the state vector $x = [\varphi_0, \ldots, \varphi_L, \omega_0, \ldots, \omega_L]^T \in \mathbb{R}^{2(n+1)}$, the electromechanical system can be represented in state-space as follows:

$$\begin{aligned} \dot{x} &= Ax + B_1 u + B_2 \tau_{fr}(\dot{\varphi}_L), \\ &= \begin{bmatrix} 0 & I \\ S & R \end{bmatrix} x + \begin{bmatrix} 0 \\ B_u \end{bmatrix} u + \begin{bmatrix} 0 \\ B_{fr} \end{bmatrix} \tau_{fr}(\dot{\varphi}_L), \end{aligned} \tag{8}$$

where $A \in \mathbb{R}^{2(n+1)\times 2(n+1)}$, $B_1 \in \mathbb{R}^{2(n+1)\times 1}$, $B_2 \in \mathbb{R}^{2(n+1)\times 1}$ are the associated system matrices, and $I \in \mathbb{R}^{(n+1)\times(n+1)}$ is the identity matrix.

Considering the angular velocity of the first mass as the measured output signal $y = \dot{\varphi}_0$, the output equation yields

$$\begin{aligned} y &= Cx, \\ &= \begin{bmatrix} 0 & \cdots & 0 & 1 & \cdots & 0 \end{bmatrix} \begin{bmatrix} \varphi_0 & \cdots & \varphi_L & \omega_0 & \cdots & \omega_L \end{bmatrix}^T, \end{aligned} \tag{9}$$

where $C \in \mathbb{R}^{1\times 2(n+1)}$ is the corresponding output matrix.

In order to perform linear analysis and control design, the high-order nonlinear model (8) and (9) can be linearized for a fixed slope of the friction curve k_{fr} as follows:

$$\dot{x} = A_d x + B_1 u, \tag{10}$$

$$y = Cx. \tag{11}$$

Here, the system matrix $A_d \in \mathbb{R}^{2(n+1)\times 2(n+1)}$ comprises a new damping matrix $R_d \in \mathbb{R}^{(n+1)\times(n+1)}$, which replaces R. This matrix is calculated in the same way as R with a new boundary damping coefficient

$$d_2 = b_2 \left[\frac{2k_{fr}}{\gamma h} + 1 \right].$$

The model parameters used for simulations are summarized in Table 1. The presented dynamic models are implemented in Matlab and calculated using the variable-step *ode*15*s* solver.

Table 1. Model parameters.

Name	Symbol	Value	Unit
Density of the motor shaft	ϱ	8000	[kg/m^3]
Shear modulus of the motor shaft	G	79.3×10^9	[N/m^2]
Structural damping of the motor shaft	γ	5×10^{-4}	[Nms]
Length of the motor shaft	L	1500	[m]
Moment of inertia of the motor shaft	I	1×10^{-5}	[m^4]
Moments of inertia of the first mass	J_1	150	[kg m^2]
Moments of inertia of the second mass	J_2	1500	[kg m^2]
Viscous friction on the first mass	β	2000	[Nms]
Coulomb friction torque	τ_{co}	165	[Nm]
Viscous dissipation torque	τ_{vi}	20	[Nms]
Static friction torque	τ_{st}	515	[Nm]
Stribeck parameter	b_{sb}	0.5	[−]
Slope in the region of zero velocity	k_{fr}	−75	[−]

3. Friction-Induced Self-Excited Oscillations

3.1. Stability and Zero Dynamics

The relative degree and zero dynamics of a system are important properties for control design. For the single-input single-output linear time-invariant system

$$\dot{x} = Ax + Bu, \tag{12}$$
$$y = Cx, \tag{13}$$

the relative degree can be obtained as the difference between the denominator and numerator polynomials orders $\nu = d - m$ of the transfer function

$$P(s) = C(sI - A)^{-1}B = \frac{a_m s^m + a_{m-1}s^{m-1} + \cdots + a_0}{s^d + b_{d-1}s^{d-1} + \cdots + b_0} \tag{14}$$

or as the smallest positive number which satisfies

$$CA^{\nu-1}B \neq 0. \tag{15}$$

The concept of zero dynamics for a linear system is equivalent to the zeros of the associated transfer function $P(s)$ [28]. The location of the zeros in the complex plane determines the stability of the zero dynamics. The system is known to be (strictly) minimum phase if the zeros z_i of $P(s)$ are in the left-half plane (LHP) Re $[z_i] \leq 0$ (Re $[z_i] < 0$).

From a theoretical point of view, the source of instability and nonminimum phase in the model (10) and (11) is the appearance of a negative slope coefficient k_{fr} for certain regions of the friction loading curve. In Figure 2 (left), the friction curve with Stribeck effect (4) is illustrated. Here, the negative slope region can be seen for small angular velocities up to 5 rad/s.

To analyze the stability of the open-loop linear plant and its zero dynamics (10) and (11), the pole-zero maps for varying slope coefficients $-100 < k_{fr} < 20$ are obtained and represented in Figure 2 (right). Here, it can be seen that the slope variation has a strong impact on the location of one real pole and one low-frequency complex conjugated pair of poles and zeros, while the dynamics of the higher-frequency modes is not affected. The low-frequency complex zero pair moves into the right-half plane (RHP), i.e., the system becomes nonminimum phase, for small slopes coefficients $k_{fr} < -5$. It can be also seen that the real pole moves into the RHP for $k_{fr} < -15$ resulting in unstable system dynamics. As depicted in Figure 2 (left, red), the region of unstable operating points is $\dot{\varphi}_L \approx 0.1 \ldots 4$ rad/s.

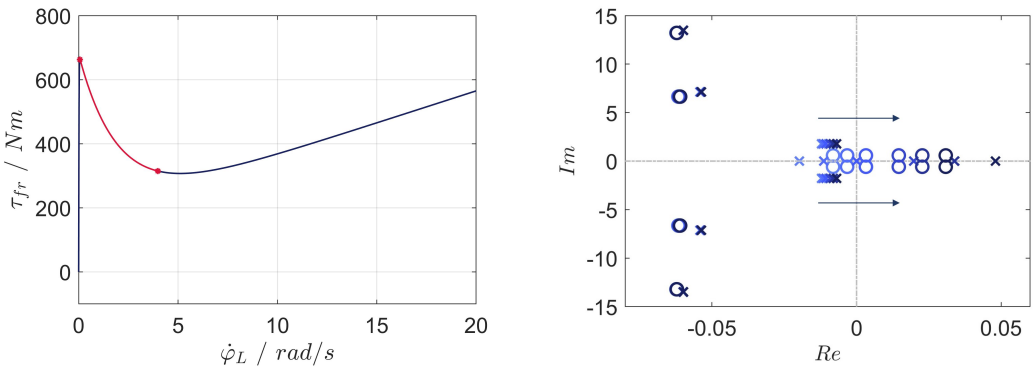


Figure 2. Friction curve (**left**): region of unstable operating points (red). Low-frequency part of pole-zero map of linearized systems (**right**).

3.2. Conventional Velocity Control

Currently, most modern mechanisms and machines are equipped with automated electric drive systems. Manufacturers of those systems typically offer a complex product with an individual software solution, e.g., a power converter with a fully parameterizable motion control system. Velocity control is one of the typical tasks for industrial systems. Due to simplicity in design and high robustness, the cascade control scheme with P/PI-controllers, depicted in Figure 3, have found wide practical application. Direct velocity measurements on the effector of the mechanism are often complicated and involve additional costs. Alternatively, they can be provided on the motor shaft via incremental or optical sensors. Therefore, for the presented system it means that only the first mass angular velocity $\dot{\varphi}_0$ is measured. From a theoretical point of view, this choice of system output for systems with more than one masses and distributed states induces zero dynamics [28]. As has been illustrated in Figure 2 (right), for systems operating in the negative slope region of a friction curve problems of unstable zero dynamics may occur.

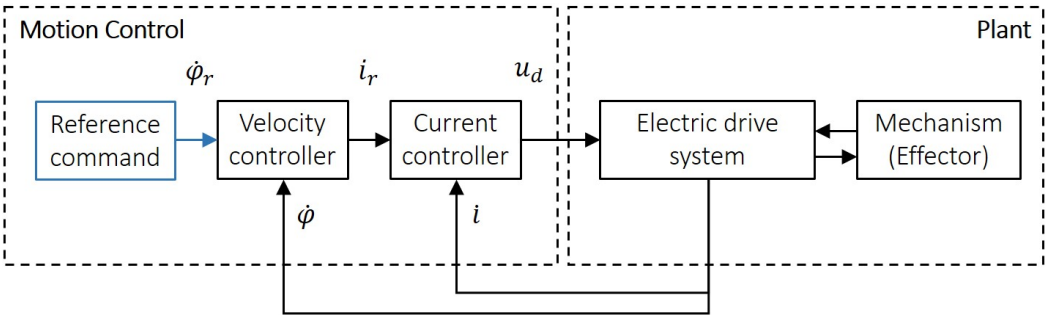


Figure 3. Conventional velocity control system.

To show the significance of the zero dynamics problem, the stability properties of the linearized system (10) and (11) with conventional velocity PI-controller

$$G_{PI}(s) = k_P \cdot \left(\frac{T_I\, s + 1}{T_I\, s}\right) \tag{16}$$

has been studied. Here, the electromechanical system is assumed to be operated at a operating velocity $\dot{\varphi} = 2$ rad/s with a slope coefficient $k_{fr} = -75$. The open-loop system in this configuration has a relative degree $\nu = 1$. In Figure 4, the low-frequency part of the root locus for fixed integral time constant $T_I = 0.8$ s and varying gain k_p is illustrated. Here, from Figure 4 (right), it can be seen that the angular velocity output and internal system dynamics can be asymptotically stabilized for a range of gains $k_P = 90 \ldots 1500$. However, this gain tuning yields poor closed-loop dynamics, as shown via simulations of the nonlinear system (Figure 5) for $k_p = 405$ (Figure 4, green poles). For higher gains, e.g., $k_P = 2 \times 10^5$, the system poles are further attracted to the system zeros (Figure 4, red poles) resulting in unstable system dynamics. This instability is a local property for the linearized system, resulting more globally in a limit cycle, i.e., nonlinear oscillations. These friction-induced self-excited oscillations can be seen in Figure 6. Here, application of a high gain $k_P = 2 \times 10^5$ leads to an approximate poles-zero pairs cancellation, which results in a stabilized angular velocity for the first mass $\dot{\varphi}_0$. However, due to presence of the unstable zero dynamics, the oscillations of the second mass velocity $\dot{\varphi}_L$ occur.

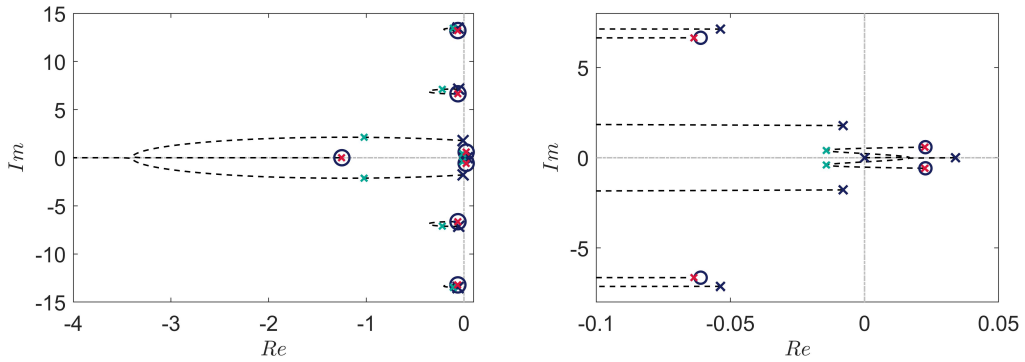


Figure 4. Low-frequency part of root locus of closed-loop system (**left**) and its zoomed-in view for the 4 low-frequency modes (**right**). Poles of the open-loop system (blue), poles of the closed-loop system with $k_P = 405$ (green), poles of the closed loop system with $k_P = 2 \times 10^5$ (red).

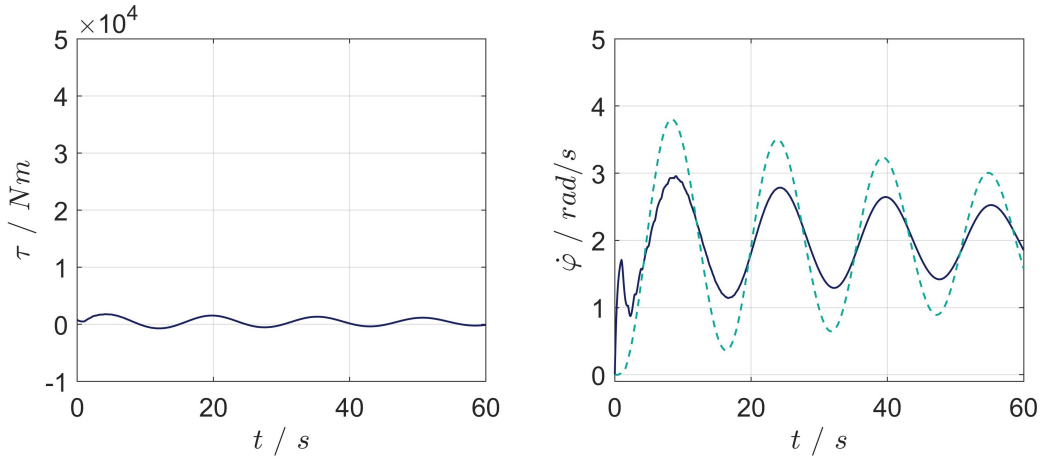


Figure 5. Step responses of the closed-loop nonlinear system applying velocity PI-controller with gain $k_P = 405$: first mass φ_0 (solid blue) and second mass φ_L (dotted green).

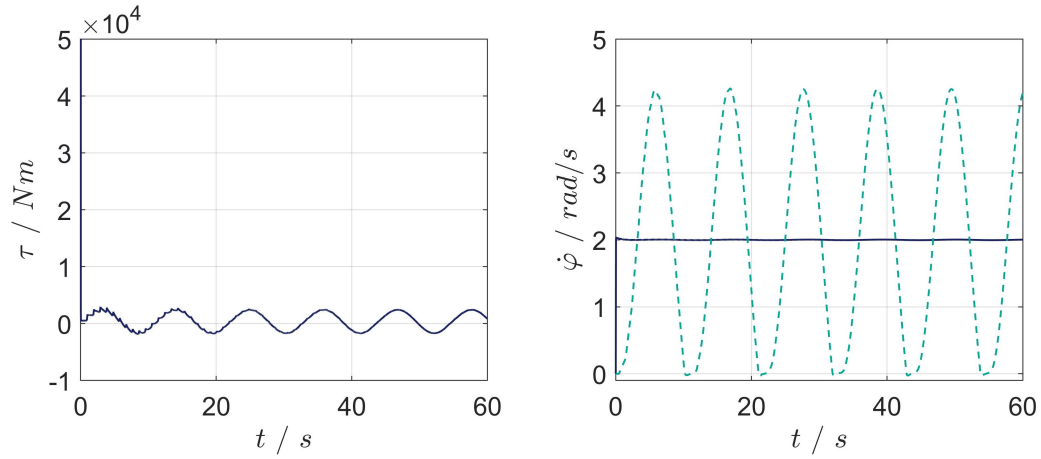


Figure 6. Step responses of the closed-loop nonlinear system applying velocity PI-controller with gain $k_P = 2 \times 10^5$: first mass φ_0 (solid blue) and second mass φ_L (dotted green).

4. PFC-Based Control

4.1. Motivation

As has been discussed above, friction loads in electromechanical systems may cause significant problems for conventional motion control systems, which can result in instabilities and the occurrence of undesired nonlinear oscillations. This is due to their nonmini-

mum phase behavior or the unstable zero dynamics, which are invariant to feedback and introduce limitations to the achievable closed-loop behavior.

Classical solution approaches to overcome this problem are the redesigning of the control scheme, to find another input–output configuration or to apply observer-based state feedback. In this contribution, a different solution based on a PFC is proposed. This approach is based on an output redefinition and it does not require additional measurements nor an observer design.

The idea of PFC-based control is to extend the plant of interest P with a PFC F, which achieves desired properties for the augmented plant $P + F$, e.g., full relative degree, passivity, ASPR. This combination yields a new output $\tilde{y} = y + y_F$ (Figure 7), which is considered for further output feedback control design.

In this work, the PFC is designed to achieve ASPR properties [23,24] for the augmented system. Here, for the extended system transfer function $\tilde{P}(s)$, the following conditions should hold:

1. $\tilde{P}(s)$ is strictly the minimum phase, i.e., zeros z_i of $\tilde{P}(s)$ are in the LHP Re $[z_i] < 0$;
2. the relative degree of the system is 0 or 1.

It should be emphasized that the extended plant transfer function $\tilde{P}(s)$ can be unstable. However, due to the ASPR properties, it is always stabilizable by proportional output feedback with a sufficiently high gain. This concept is particularly useful for non-identifier-based adaptive control methods, e.g., λ-tracking control, where the stable zero dynamics plays a key role.

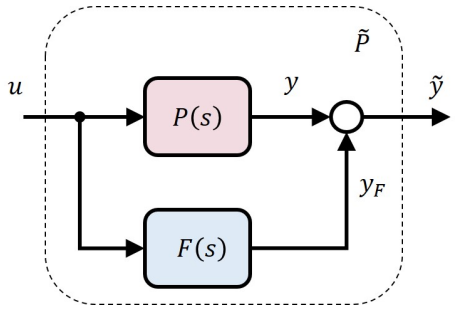


Figure 7. Parallel feed-forward interconnection: plant $P(s)$, PFC $F(s)$ and extended plant $\tilde{P}(s)$.

4.2. PFC Design

Consider the following single-input single-output linear time-invariant plant, which is a nonminimum phase and unstable

$$P(s) = \frac{y(s)}{u(s)} = \frac{M(s)}{D(s)}, \tag{17}$$

where $D(s)$ is a polynomial of degree d and $M(s)$ is a polynomial of degree $m \leq d$.

To place the system zeros for the augmented system with the output $\tilde{y}$, an appropriate PFC $F(s)$, as illustrated in Figure 7, has to be designed. In addition, the PFC $F(s)$ should not introduce a static contribution in this output.

Consider the following PFC transfer function

$$F(s) = \frac{y_F(s)}{u(s)} = \frac{sA(s)}{B(s)}, \tag{18}$$

where $B(s)$ is a polynomial of degree d and $sA(s)$ is a polynomial of degree $d - 1$, which contains the derivative to achieve a vanishing static contribution.

A parallel feed-forward interconnection of the plant and PFC results in

$$\tilde{P}(s) \quad = \quad P(s) + F(s) = \frac{sD(s)A(s) + M(s)B(s)}{D(s)B(s)}. \tag{19}$$

Here, stability of the system zeros for the extended system $\tilde{P}(s)$ is obtained if and only if the numerator polynomial $sD(s)A(s) + M(s)B(s)$ has roots only in LHP. This problem can be directly solved by equating the numerator polynomial to a desired polynomial $L_d(s)$ of a suitable degree

$$sD(s)A(s) + M(s)B(s) = L_d(s)\,, \tag{20}$$

and finding the corresponding coefficients of $A(s)$ and $B(s)$. The linear Diophantine Equation (20) can be solved, e.g., by applying Sylvester's matrix approach [29].

The specific choice of $L_d(s)$ is a degree of freedom in this design. Generally, it should contain only LHP roots with a desired location in the complex plane. The degree of $L_d(s)$ should be selected based on the relative degree of the transfer function $P(s)$, i.e.,

$$\deg\big(L_d(s)\big) = \begin{cases} 2d-1 & \text{if } m < d\,, \\ 2d & \text{if } m = d\,. \end{cases} \tag{21}$$

It can be seen that this design achieves for the augmented plant $\tilde{P}$ the following relative degree

$$\nu = \begin{cases} 1 & \text{if } m < d\,, \\ 0 & \text{if } m = d\,. \end{cases} \tag{22}$$

4.3. Stability of the Augmented Plant

Applying the proposed design procedure yields a PFC $F(s)$ of the same order as the plant. The order of the linearized system (10) and (11) depends directly on the number of discretization points n and is typically high. This makes computation and further practical implementation difficult. To overcome this problem, the order of the system or PFC has to be reduced. In this work, the modal truncation procedure has been applied to the high-order plant model [30]. The reduction order selection always depends on the specific application case and can be motivated using the frequency domain. In Figure 8, the Bode diagram of the linearized system is presented (blue). Here, it can be seen that mainly one unstable real pole and two low-frequency eigen-modes have a dominant impact on the system dynamics. Assuming that the higher-frequency modes are not excited by the drive system or external disturbances, a fifth-order model approximation $n_r = 5$ is chosen (green).

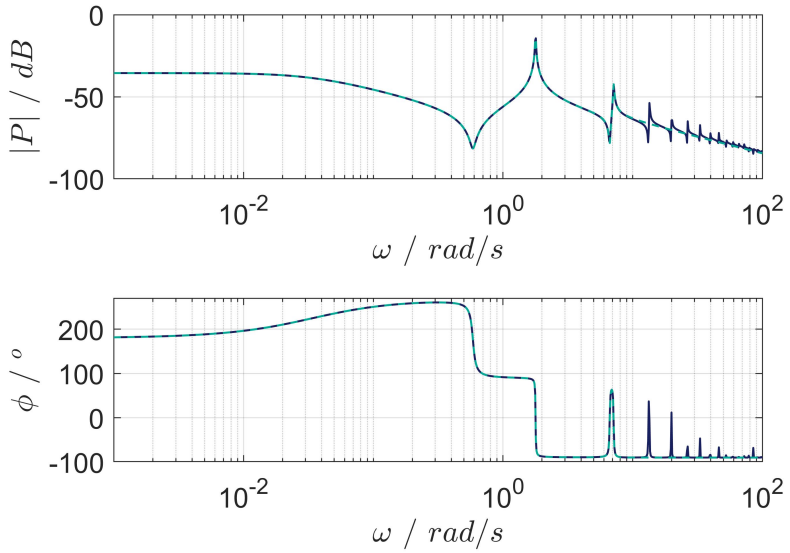


Figure 8. The Bode diagram of the linearized system. High-order model (solid blue); reduced order model (dashed green).

To design an appropriate PFC, according to (21), a desired polynomial $L_d(s)$ of degree 9 should be assigned. The numerator polynomial $sD(s)A(s) + M(s)B(s)$ contains the plant polynomials $D(s)$ and $M(s)$. Thus, the choice of the desired roots can be motivated physically. Here, the frequencies of $D(s)$ and $M(s)$ have been left unchanged. However, additional damping for the complex conjugated roots has been added. Additionally, a new location for the real root in LHP has been assigned.

$$L_d(s) = (s + 0.8)(s^2 + 0.8s + 0.3)(s^2 + 2.5s + 3.2)(s^2 + 4.7s + 44.3)(s^2 + 5s + 51). \quad (23)$$

Then, according to (20), the following PFC is obtained

$$F(s) = \frac{-0.02s(s + 17.12)(s^2 - 2.5s + 3.4)}{(s + 31.4)(s - 15.2)(s + 0.2)(s^2 + 0.84s + 3.8)}. \quad (24)$$

To analyze the linear system properties of $\tilde{P}(s)$ and stability of the closed-loop system, the root locus for varying gain k_P is calculated and depicted in Figure 9. It can be seen that applying high gains $k_P > 3.2 \times 10^3$ results in stable closed-loop dynamics. It should be emphasized that the leading coefficient of the resulting augmented plant $\tilde{P}(s)$ is negative, and for the root locus and further adaptive control an additional negative sign as multiplier for k_P and $k(t)$ is used, respectively.

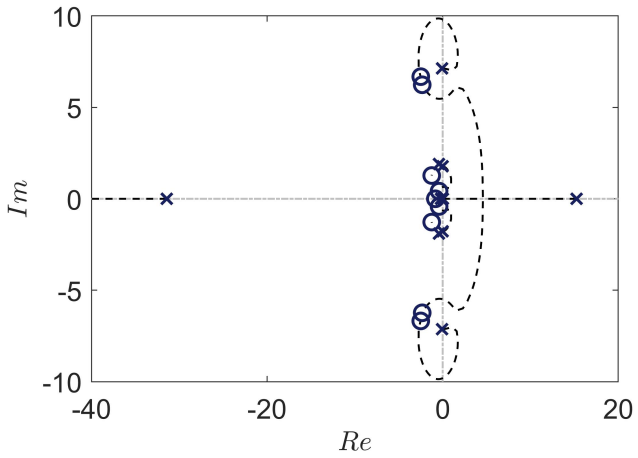


Figure 9. Root locus of the $\tilde{P}$.

4.4. PFC-Based Adaptive Feedback Control

To provide stability of the augmented system, an adaptive λ-tracking control law is used in this work. This approach is not based on a model and requires only minimal information about the system, in particular its DC gain. However, it is only applicable for certain classes of systems, including ASPR systems [20,25].

In Figure 10, the overall control scheme is presented. Here, the tracking error considering the augmented output $\tilde{y}$ is

$$e(t) = y_r(t) - \tilde{y}\,. \quad (25)$$

To control the augmented system, the following adaptive control law is applied to the augmented plant

$$u(t) = k(t)e(t)\,, \quad (26)$$

where the time-varying gain $k(t)$ is given by the parameter adaptation law

$$\begin{aligned} \dot{k}(t) &= \xi \max\left(|e(t)| - \lambda, 0\right)^2, \\ k(0) &= k_0\,. \end{aligned} \quad (27)$$

Here, λ defines the adaptation dead-zone, i.e., the control gain $k(t)$ is adapted only if $|e(t)| \geq \lambda$, ξ is the adaptation rate parameter and k_0 is the initial value of $k(t)$.

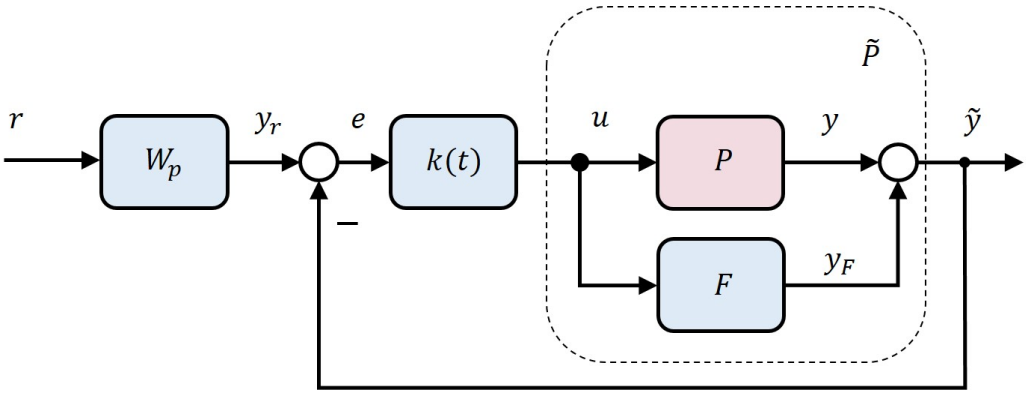


Figure 10. Overall control scheme: plant P, PFC F, precompensator W_p and adaptive λ-tracking controller $k(t)$.

To reduce overshoots in the angular velocities $\dot{\varphi}$, an additional first order precompensator W_p is utilized

$$W_p(s) = \frac{1}{T_p s + 1}, \tag{28}$$

where T_p is a time constant.

5. Results

In this section, the presented PFC-based adaptive λ-tracking control is evaluated in a simulation study. To verify in particular its robustness with respect to measurement noise and parameter uncertainties, the following simulation scenarios are considered

- Scenario 1: adaptation, angular velocity reference tracking and disturbance rejection of the closed-loop system;
- Scenario 2: adaptation and angular velocity reference tracking of the closed-loop system in the presence of measurement noise;
- Scenario 3: adaptation and angular velocity reference tracking of the closed-loop system in the presence of parameters variation.

The PFC (24) and the following parameters of the feedback control law ((26)), (27) have been utilized and applied to the discretized high-order nonlinear model ((8), (9))

- $\lambda = 0.1$ is chosen as 5% from the reference value $r = 2$ rad/s;
- $\xi = 1 \times 10^8$ is chosen to provide a reasonable adaptation rate;
- $k_0 = 1$;
- $T_p = 4$ s for the reference tracking ($T_p = 1$ s for the adaptation).

To perform the adaptation and reference tracking, the reference signal r depicted in Figure 11 (dotted gray) has been utilized for all scenarios. Initially, two pulse signals with an amplitude of 2 rad/s and width 5 s are applied to allow for an adaptation of the control gain $k(t)$ ($T_p = 1$ s). After that, at time 30 s, a step signal is applied to evaluate the reference tracking of the closed-loop system ($T_p = 4$ s).

The following performance measures are considered to evaluate transients during the reference tracking: rise time t_{rise} to 98% of the reference value, settling time t_{settle} with accuracy 2% and relative overshoot. These measures are applied to the angular velocities of the first $\dot{\varphi}_0$ and second $\dot{\varphi}_L$ masses.

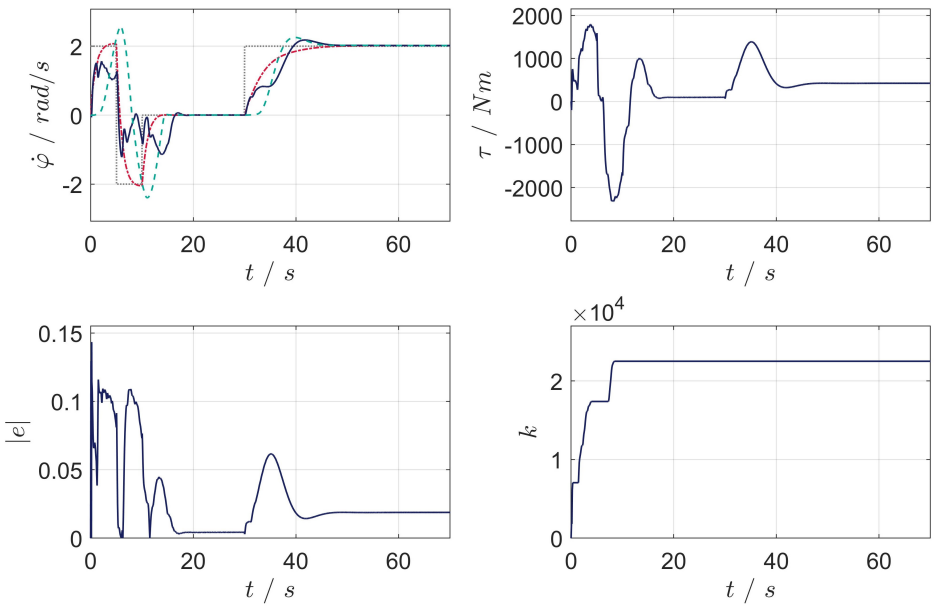


Figure 11. Transient responses of the closed-loop system. Adaptation and angular velocity reference tracking: $\dot{\varphi}_0$ (solid blue), $\dot{\varphi}_L$ (dashed green), $\tilde{y}$ (dash-dot red) and r (dotted gray).

5.1. Scenario 1

The obtained simulation results are illustrated in Figures 11–13. From Figure 11, it can be seen that the absolute value of the control error $|e(t)|$ converges to the prescribed $\lambda = 0.1$ after about 8.5 s resulting in an adapted control gain $k(t)|_{t>8.5s} = 2.25 \times 10^4$. The augmented output $\tilde{y}$ reaches the reference angular velocity value 14.2 s after the step $r(s)$ and settles without overshoot. The performance measures of the reference tracking are summarized in Tables 2 and 3 (Case 1). From Figure 12 it can be seen that not only the angular velocities on the boundaries $\dot{\varphi}_0$ and $\dot{\varphi}_L$ are stabilized, but also the distributed state $\dot{\varphi}(z,t)$ itself.

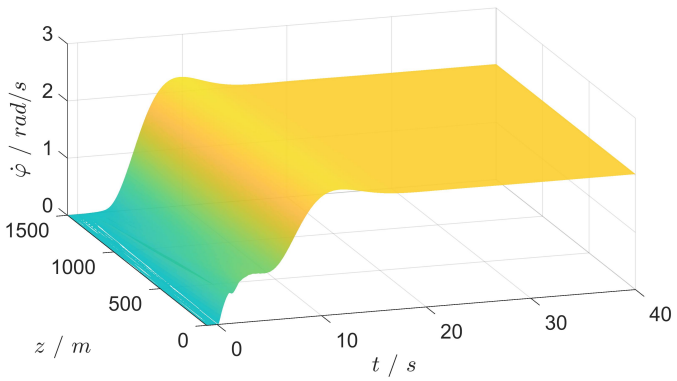


Figure 12. Transient responses of the closed-loop system. Angular velocity reference tracking: distributed $\dot{\varphi}(z,t)$.

Table 2. Performance measures for $\dot{\varphi}_0$.

Cases	1	2	3	4	5	6	7	8	9
t_{rise} $[s]$	9.27	8.22	10.46	9	12.25	9.92	9.80	8.68	11.15
t_{set} $[s]$	16.62	21.15	20.64	16.11	13.94	20.15	17.12	28.07	21.25
σ [%]	8.97	4.32	15.08	5.53	2.04	12.01	12.96	9.48	18.52

Table 3. Performance measures for $\dot{\varphi}_L$.

Cases	**1**	**2**	**3**	**4**	**5**	**6**	**7**	**8**	**9**
t_{rise} $[s]$	7.44	6.40	8.62	7.26	10.46	8.12	7.91	6.71	9.28
t_{set} $[s]$	15	19.26	23.03	14.90	14.18	18.51	15.22	26.26	34.05
σ $[\%]$	12.74	5.38	22.79	7.44	1.92	18	19.03	11.57	28.19

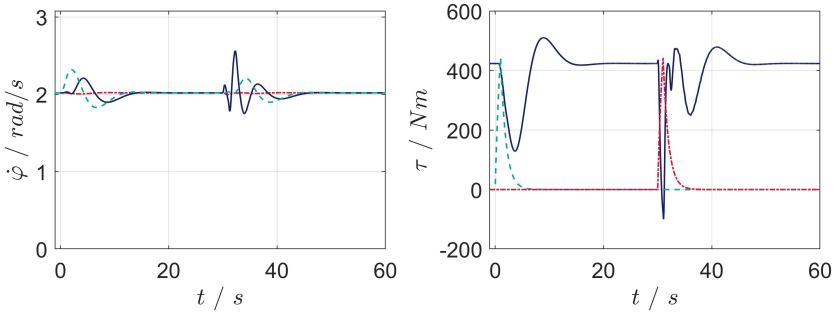


Figure 13. Transient responses of the closed-loop system. Disturbance rejection: $\dot{\varphi}_0$ (solid blue), $\dot{\varphi}_L$ (dashed green) and $\tilde{y}$ (dash-dot red). Impulse torques are applied to the second mass at time $t_1 = 0$ s (dashed green) and to the first mass $t_1 = 30$ s (dash-dot red).

In Figure 13, the disturbance rejection of the closed-loop system are shown. Here, two impulse disturbance torques are applied to the first and the second masses (Figure 13, right). In both cases the disturbances are suppressed notably within about 15 s.

5.2. Scenario 2

In this scenario, the control law adaptation and reference tracking in the presence of measurement noise are shown. To introduce the measurement noise, a Gaussian distributed random signal with variance of $\sigma^2 = 2.5 \times 10^{-5}$ is utilized. The noise is applied to the measured angular velocity on the first mass $y = \varphi_0$. The obtained results are illustrated in Figure 14. Here, it can be seen that application of the noise does not deteriorate the adaptation of the control gain $k(t)$. In general, the measurement noise is evaluated from the transient response of $|e|$ and the corresponding parameter λ is chosen. It should be also emphasized that the high control gains boost the measurement noise considerable. This typically results in faster wear of the actuator and reduced performance [31]. To overcome this problem, an additional low-pass filter for noise signals with a larger variances is needed.

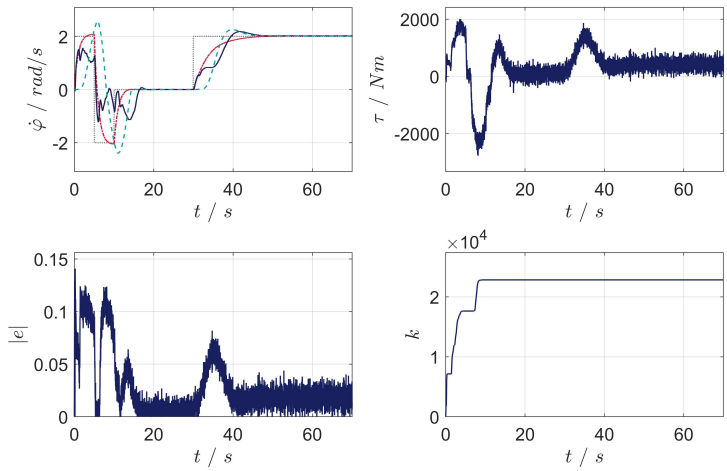


Figure 14. Transient responses of the closed-loop system. Adaptation and angular velocity reference tracking in presence of the measurement noise: $\dot{\varphi}_0$ (solid blue), $\dot{\varphi}_L$ (dashed green), $\tilde{y}$ (dash-dot red) and r (dotted gray).

5.3. Scenario 3

In this scenario, evaluation of the robustness with respect to parameter uncertainties is shown. To introduce the parameter uncertainties, the following parameters variation are considered:

- The static friction torque τ_{st} from (4) is varied in a range of $\pm 50\%$ from its nominal value resulting in a different slope of the friction curve in the operating point of interest;
- The moment of inertia of the second mass J_2 is varied in a range of $\pm 50\%$ from its nominal value.

The domain of uncertain parameters is illustrated in Figure 15. Here, the nominal and worst cases of parameter variations are denoted with numbers. The nominal case 1 and following worst cases 2–9 have been used for the simulation study.

Assuming the model parameters are varying according to cases 2–9 and the control system parameters designed for the nominal case 1 remain constant, the following results are obtained and depicted Figure 16. Here, it can be seen that although in certain cases the performance of the transients has slightly deteriorated, the closed-loop system is always stable. From a theoretical point of view, this means that the designed PFC provides stability of the zero dynamics even for these worst case variations and, hence, the overall control system is robust to these parameter variations. The performance measures of the reference tracking for all cases are summarized in Tables 2 and 3.

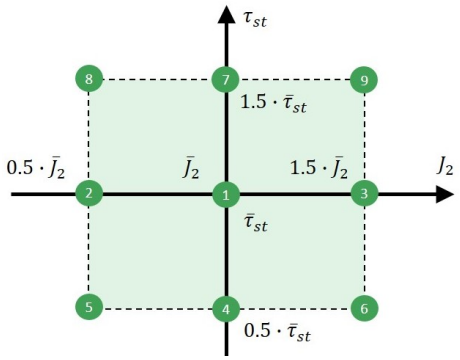


Figure 15. Domain of parameters variation and simulation cases.

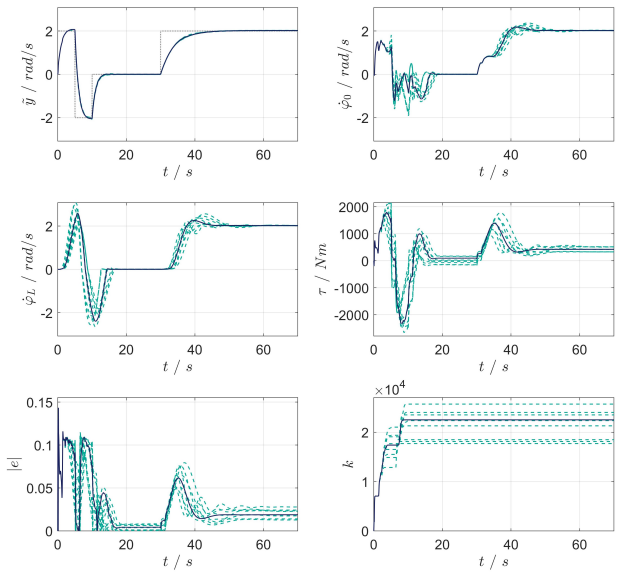


Figure 16. Transient responses of the closed-loop system. Adaptation and angular velocity reference tracking in presence of parameter uncertainties: nominal parameter model (solid blue) and uncertain parameter model (dashed green).

6. Conclusions

In this contribution, the PFC-based adaptive λ-tracking control is proposed for velocity control of an electromechanical system with friction load. The mathematical model of a two-mass electromechanical system with an elastic shaft and a friction load with the Stribeck effect has been studied. It has been shown that under certain conditions the system becomes a nonminimum phase and unstable. Practically, applying a conventional control system may result in the occurrence of friction-induced self-excited oscillations. To overcome this problem without additional measurements nor observers, an alternative approach based on a PFC has been introduced. The proposed PFC design renders the augmented plant ASPR, i.e., stable zero dynamics and a relative degree of one. Further application of the adaptive λ-tracking controller results in stable closed-loop system dynamics. The performance of the proposed control system has been successfully evaluated in a simulation study.

In this work, the robustness of the proposed approach is analyzed in the simulation study. For further applications, a robust PFC design that takes into account model uncertainties will be proposed. In addition, the future work will be concerned with a practical verification of the proposed approach.

Author Contributions: Conceptualization, S.P.; methodology, S.P.; software, I.G.; validation, I.G. and S.P.; formal analysis, I.G. and S.P.; investigation, I.G. and S.P.; data curation, I.G.; writing—original draft preparation, I.G.; writing—review and editing, S.P.; visualization, I.G.; supervision, S.P. All authors have read and agreed to the published version of the manuscript.

Funding: This research received no external funding.

Data Availability Statement: Not applicable.

Conflicts of Interest: The authors declare no conflict of interest.

Abbreviations

The following abbreviations are used in this manuscript:

PFC	Parallel feed-forward compensator
ASPR	Almost strictly positive real
PDE	Partial differential equation
RHP	Right-half plane
LHP	Left-half plane

References

1. Armstrong-Hélouvry, B.; Dupont, P.; De Wit, C.C. A survey of models, analysis tools and compensation methods for the control of machines with friction. *Automatica* **1994**, *30*, 1083–1138. [CrossRef]
2. Olsson, H.; Åström, K.J.; Gafvert, M.; Lischinsky, P.; Canudas de Wit, C. Friction Models and Friction Compensation. *Eur. J. Control* **1998**, *4*, 176–195. [CrossRef]
3. Keck, A.; Zimmermann, J.; Sawodny, O. Friction parameter identification and compensation using the ElastoPlastic friction model. *Mechatronics* **2017**, *47*, 168–182. [CrossRef]
4. Nechak, L. Nonlinear state observer for estimating and controlling of friction-induced vibrations. *Mech. Syst. Signal Process.* **2020**, *139*, 106588. [CrossRef]
5. Klepikov, V. *Dynamics of Electromechanical Systems with Nonlinear Friction (in Russian)*; NTU "KhPI": Kharkiv, Ukraine, 2014.
6. Mihajlović, N. Torsional and Lateral Vibrations in Flexible Rotor Systems with Friction. Ph.D. Thesis, Technische Universiteit Eindhoven, Eindhoven, The Netherlands, 2005.
7. Cui, X.; Huang, B.; Du, Z.; Yang, H.; Jiang, G. Study on the Mechanism of the Abnormal Phenomenon of Rail Corrugation in the Curve Interval of a Mountain City Metro. *Tribol. Trans.* **2020**, *63*, 996–1007. [CrossRef]
8. Wang, C.; Ayalew, B.; Adcox, J.; Dailliez, B.; Rhyne, T.; Cron, S. Self-excited torsional oscillations under locked-wheel braking: Analysis and experiments. *Tire Sci. Technol.* **2015**, *43*, 276–296. [CrossRef]
9. Berthold, C.; Gross, J.; Frey, C.; Krack, M. Development of a fully-coupled harmonic balance method and a refined energy method for the computation of flutter-induced Limit Cycle Oscillations of bladed disks with nonlinear friction contacts. *J. Fluids Struct.* **2021**, *102*, 103233. [CrossRef]
10. Papangelo, A.; Putignano, C.; Hoffmann, N. Self-excited vibrations due to viscoelastic interactions. *Mech. Syst. Signal Process.* **2020**, *144*, 106894. [CrossRef]

11. Liu, J.; Xu, Y.; Pan, G. A combined acoustic and dynamic model of a defective ball bearing. *J. Sound Vib.* **2021**, *501*, 116029. [CrossRef]
12. Marquez, M.B.S.; Boussaada, I.; Mounier, H.; Niculescu, S.I. *Analysis and Control of Oilwell Drilling Vibrations: A Time-Delay Systems Approach*; Springer: Heidelberg, Germany, 2015.
13. Lin, Wei.; Liu, Yang. Proportional-Derivative Control of Stick-Slip Oscillations in Drill-Strings. *MATEC Web Conf.* **2018**, *148*, 16005. [CrossRef]
14. Ritto, T.; Ghandchi-Tehrani, M. Active control of stick-slip torsional vibrations in drill-strings. *J. Vib. Control* **2019**, *25*, 194–202. [CrossRef]
15. Puebla, H.; Alvarez-Ramirez, J. Suppression of stick-slip in drillstrings: A control approach based on modeling error compensation. *J. Sound Vib.* **2008**, *310*, 881–901. [CrossRef]
16. Wasilewski, M.; Pisarski, D.; Konowrocki, R.; Bajer, C.I. A New Efficient Adaptive Control of Torsional Vibrations Induced by Switched Nonlinear Disturbances. *Int. J. Appl. Math. Comput. Sci.* **2019**, *29*, 285–303. [CrossRef]
17. Chomette, B.; Sinou, J.J. On the Use of Linear and Nonlinear Controls for Mechanical Systems Subjected to Friction-Induced Vibration. *Appl. Sci.* **2020**, *10*, 2085. [CrossRef]
18. Sadeghimehr, R.; Nikoofard, A.; Sedigh, A.K. Predictive-based sliding mode control for mitigating torsional vibration of drill string in the presence of input delay and external disturbance. *J. Vib. Control* **2020**. [CrossRef]
19. Ullah, F.K.; Duarte, F.; Bohn, C. A novel backstepping approach for the attenuation of torsional oscillations in drill strings. In *Solid State Phenomena*; Trans Tech Publications Ltd.: Freienbach, Switzerland , 2016; pp. 85–92.
20. Bar-Kana, I. Parallel feedforward and simplified adaptive control. *Int. J. Adapt. Control. Signal Process.* **1987**, *1*, 95–109. [CrossRef]
21. Palis, S.; Kienle, A. Discrepancy based control of particulate processes. *J. Process Control* **2014**, *24*, 33–46. [CrossRef]
22. Kim, H.; Kim, S.; Back, J.; Shim, H.; Seo, J.H. Design of stable parallel feedforward compensator and its application to synchronization problem. *Automatica* **2016**, *64*, 208–216. [CrossRef]
23. Barkana, I. Positive-realness in discrete-time adaptive control systems. *Int. J. Syst. Sci.* **1986**, *17*, 1001–1006. [CrossRef]
24. Iwai, Z.; Mizumoto, I.; Mingcong D. A parallel feedforward compensator virtually realizing almost strictly positive real plant. In Proceedings of the 1994 33rd IEEE Conference on Decision and Control, Lake Buena Vista, FL, USA, 14–16 December 1994; Volume 3, pp. 2827–2832.
25. Hackl, C. *Non-Identifier Based Adaptive Control in Mechatronics*; Springer: Berlin/Heidelberg, Germany, 2017.
26. Koser, K.; Pasin, F. Torsional Vibrations of the Drive Shafts of Mechanisms. *J. Sound Vib.* **1997**, *199*, 559–565. [CrossRef]
27. Schiesser, W.E.; Griffiths, G.W. *A Compendium of Partial Differential Equation Models: Method of Lines Analysis with Matlab*; Cambridge University Press: Cambridge, UK, 2009.
28. Isidori, A. The zero dynamics of a nonlinear system: From the origin to the latest progresses of a long successful story. *Eur. J. Control* **2013**, *19*, 369–378. [CrossRef]
29. Goodwin, G.C.; Graebe, S.F.; Salgado, M.E. *Control System Design*, 1st ed.; Prentice Hall PTR: Hoboken, NJ, USA, 2000.
30. Golovin, I.; Palis, S. Robust control for active damping of elastic gantry crane vibrations. *Mech. Syst. Signal Process.* **2019**, *121*, 264–278. [CrossRef]
31. Segovia, V.R.; Hägglund, T.; Åström, K. Measurement noise filtering for PID controllers. *J. Process Control* **2014**, *24*, 299–313. [CrossRef]